Resonant and nonresonant scattering of dipole-dominated spin waves from a region of inhomogeneous magnetic field in a ferromagnetic film

M. P. Kostylev,[1,2,*] A. A. Serga,[1,†] T. Schneider,[1] T. Neumann,[1] B. Leven,[1] B. Hillebrands,[1] and R. L. Stamps[2]
[1]*Department of Physics and Forschungsschwerpunkt MINAS, Technische Universität Kaiserslautern, D-67663 Kaiserslautern, Germany*
[2]*School of Physics, M013, University of Western Australia, Stirling Highway, Crawley, Western Australia 6009, Australia*
(Received 7 June 2006; revised manuscript received 31 July 2007; published 15 November 2007; corrected 19 November 2007)

The transmission of a dipole-dominated spin wave in a ferromagnetic film through a localized inhomogeneity in the form of a magnetic field produced by a dc through a wire placed on the film surface was studied experimentally and theoretically. It was shown that the amplitude and phase of the transmitted wave can be simultaneously affected by the current induced field, a feature that will be relevant for logic based on spin wave transport. The direction of the current creates either a barrier or a well for spin wave transmission. The main observation is that the current dependence of the amplitude of the spin wave transmitted through the well inhomogeneity is nonmonotonic. The dependence has a minimum and an additional maximum. A theory was constructed to clarify the nature of the maximum. It shows that the transmission of spin waves through the inhomogeneity can be considered as a scattering process and that the additional maximum is a scattering resonance.

DOI: 10.1103/PhysRevB.76.184419 PACS number(s): 75.50.Cc, 75.30.Ds, 75.40.Gb

INTRODUCTION

The topic of dipole-dominated spin waves (SWs) in confined geometries, such as ferromagnetic stripes and dots, is currently receiving great deal of attention because of possible applications for data storage and processing (see, e.g., Ref. 1 and extensive literature referenced therein). The field has grown dramatically in the past few years, due in part to advances in nanoscale engineering that make it now possible to pattern periodic arrays of elements sufficiently dense that elements interact via stray dipolar fields.[2–7] One consequence is that propagating collective spin wave modes supported by dynamic dipole fields can be experimentally observed and studied.[8] Understanding the dynamics of these excitations is important for a number of phenomena, including fast field or current driven switching.

Propagating collective modes in these systems can be considered as a particular case of the more general phenomenon of scattering of a spin wave from a large inhomogeneity in a planar geometry. Typical length scales mean that spin waves can tunnel between and through elements, or exist as confined modes within elements.

The first studies of spin wave scattering appeared in the 1980s, with an emphasis on refraction effects (see, Refs. 9–11 and other numerous works by the same authors). Scatterers in these and other studies were constructed by applying slowly spatially varying static magnetic field or by depositing thin metallic layers on the surface of the film.[11–18] Scattering from other static inhomogeneities in the form of periodical variations such as saturation magnetization or magnetostriction were also studied.[19] Some years ago, Bragg scattering from a spatially modulated magnetic field was reported.[20,21]

More recently, tunneling of dipole-dominated spin waves through a reststrahl region created by a locally applied magnetic field was demonstrated.[22] This region behaves much like a barrier to spin wave propagation and can be controlled through the magnitude of the magnetic field creating the inhomogeneity. In contrast to the previous studies, in this work the inhomogeneity was *highly localized* in a sense that its length was of several wavelengths or less of the spin wave incident onto it. For this purpose, the local magnetic field is created by a dc flowing through a wire of diameter of several dozens of micrometers placed on top of the film. In this way, it is also possible to control the amplitude of the transmitted wave electrically [an example is sketched in Fig. 1(a)]. Furthermore, the magnetic field can be modulated on nanosecond time scales. This makes the phenomena very interesting from point of view of applications, especially for signal processing at gigahertz frequencies.

What is most interesting perhaps is that either a barrier or a well can be created simply by changing the direction of the current. In particular, in the case of backward volume magnetostatic waves (BVMSWs), a barrier is produced with a current that subtracts from the local field in the magnetic film and a well is produced by a current that produces a field which adds to the local field in the film. These effects are illustrated in Figs. 1(b) and 1(c). Propagation of BVMSWs through the barrier is not possible except via tunneling,[22] but propagation across the well introduces a phase shift and partial reflection (except for resonances which are discussed in detail later).

The purpose of this paper is to investigate experimentally and theoretically the transmission of dipole-dominated spin waves in a ferromagnetic film through a nonperiodic highly localized inhomogeneity in a ferromagnetic film. Whereas we are primarily concerned with inhomogeneities created by a dc through a thin wire on the surface of a magnetic film, our results apply generally for any one-dimensional scalar inhomogeneity. We treat the propagation of spin waves through a region of magnetic inhomogeneity as a one-dimensional scattering problem. By analogy to quantum mechanical scattering of a particle from a potential well, scattering resonances can take place for certain spin wave wavelengths. If the well has smooth boundaries, as created by the Oersted field of the wire, the resonance condition is not trivial.

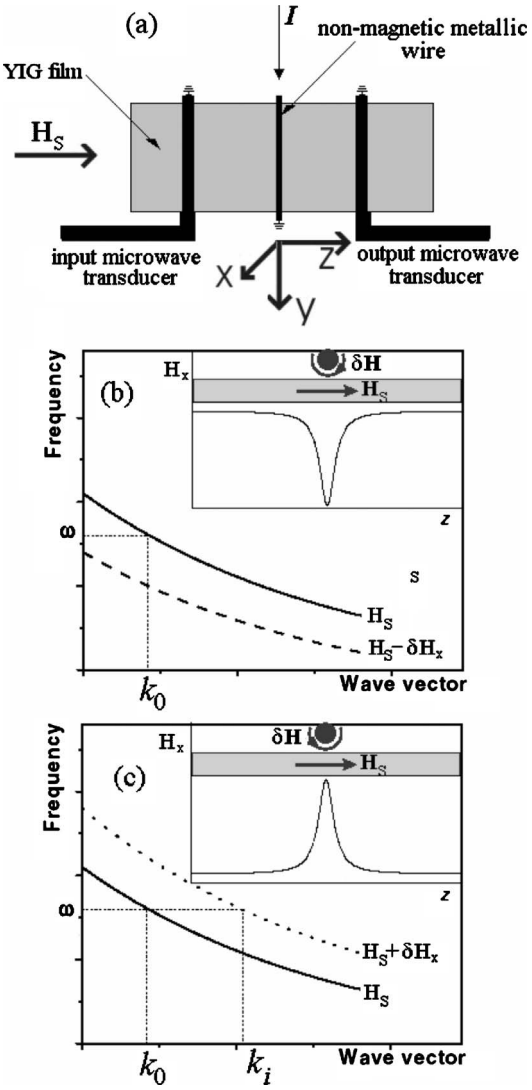

FIG. 1. (a) Structure under investigation. The origin of the frame of reference coincides with the longitudinal symmetry axis of the wire. (b) Dip-shaped profile of the static magnetic field and BVMSW downshift of the dispersion in the regime of tunneling. (c) Hump-shaped profile of the static field and upshift of the BVMSW dispersion in the regime of scattering. Solid lines: Dispersion outside the inhomogeneity. Dashed line in (b) and dotted line in (c): Dispersion inside the inhomogeneity.

A new possible application of linear spin waves is the recently proposed SW logic.[23,24] The logic is based on the control of the spin wave phase. In the latter paper, the control was achieved by varying the static magnetic field produced by a dc through a wide magnetic stripe placed on the ferromagnetic-film sample. This allowed construction of a logic NOT gate. Both Refs. 23 and 24 used the same idea of wave interferometer for transformation of phase modulation of spin wave induced by the dc into amplitude modulation of the device output signal.

A more direct way would be to directly control the spin wave amplitude. The scattering and/or tunneling of spin waves through a highly localized inhomogeneity provides such a possibility. Indeed, the experimental structure in Ref. 22 represents a NOT gate. However, to construct more sophisticated universal logical gates, such as the NAND gate, a control of both phase and amplitude is needed simultaneously. In this regard, the focus of this paper is on how current controlled tunneling and transmission affects both amplitude and phase of the scattered spin wave.

The paper is organized as follows. In Sec. I, we describe the results of experimental investigation of BVMSW propagation through an inhomogeneity of static magnetic field in an yttrium iron garnet film. We show that the dependence of amplitude of the wave transmitted through the localized inhomogeneity depends nonmonotonically on the inhomogeneity height. To find the origin of this unexpected nonmonotonic behavior in Sec. II we construct a theory of dipole-dominated spin wave scattering from a one-dimensional (1D) inhomogeneity. In Sec. III, the theory is applied to explain this and other experimentally observed peculiarities of BVMSW propagation through the inhomogeneity. Appendixes A and B contain details of the derivation of the final equations given in Sec. II and used for calculations in Sec. III.

I. EXPERIMENT

We consider the structure shown in Fig. 1(a). Microwave spin wave packets in an yttrium iron garnet film with thickness of 4.9 μm are excited by microwave current pulses in a strip-line transducer. They are detected by a second transducer placed at 8 mm apart from the first one. Both a homogeneous external field $\mathbf{H}_s$ and the static magnetization $\mathbf{M}_s$ are oriented in the plane of the film parallel to the propagation direction of spin waves, z. The dynamic magnetization has an in-plane component, m_y, and an out-of-plane component, m_x. The propagation direction relative to the saturation magnetization ensures that backward volume magnetostatic spin waves are produced which are characterized by a negative group velocity.[25]

The microwave part of the measurement setup consists of a microwave generator and a switch, which is controlled by a pulse generator (pulse length of 320–1600 ns) and connected to the input transducer. BVMSW pulses are generated with a carrier frequency $\omega/(2\pi)=7.125$ GHz and a carrier wave vector $k_0=49-267$ rad/cm, the value of k_0 being determined by the dispersion relation for BVMSW in an external field.

A narrow gold wire of circular cross section of 25 μm in diameter is mounted across the film parallel to transducers, 4 mm apart from the input transducer. The wire carries a dc I. It is used to create a local inhomogeneous field $\delta\mathbf{H}(z)$. Depending on the direction of the dc, the total field is locally reduced [Fig. 1(b)] or enhanced [Fig. 1(c)] by the Oersted field of the current. The negative group velocity of the backward volume magnetostatic wave[25] means that frequency decreases with increasing wave number. An increase of the static field shifts the manifold of allowed frequencies up [Fig. 1(c)], and a decrease in the field shifts the manifold down [Fig. 1(b)]. Therefore, a local decrease of the magnetic field means that the carrier frequency of the wave incident on the inhomogeneity falls outside of the spin wave manifold

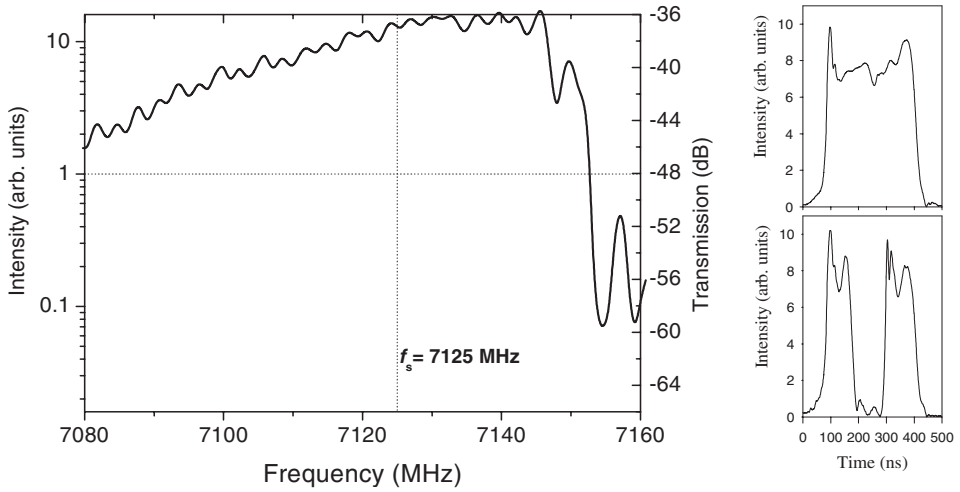

FIG. 2. Raw experimental data. Left panel: Amplitude frequency characteristic measured in cw regime. Right panels: Intensity profiles for the pulses used in the measurements of the amplitude of the complex transmission coefficient (upper graph, No dc applied; lower graph, I=0.5 A).

into the spin wave reststrahl region. Propagation in this region is not possible, but a spin wave can tunnel through this inhomogeneity if it is sufficiently narrow.[22]

If the magnetic field is increased locally, the inhomogeneity takes the form of a well and merely shifts the position of the spin wave carrier frequency within the spin wave manifold. Propagation of BVMSW is allowed if the field locally does not exceed the value corresponding to the lower boundary of spin wave manifold. In order to propagate through the inhomogeneity, the carrier wave number of incident wave will adjust since the frequency remains constant, thereby resulting in a phase shift of the transmitted wave. Reflection can occur, and this decreases the power transmitted through the inhomogeneity. This provides the basic mechanism whereby both phase and amplitude can be adjusted by varying details of the current induced inhomogeneity.

To measure the transmission coefficient of the inhomogeneity, the output microwave signal from the output transducer is monitored by a microwave detector and visualized on an oscilloscope. To measure the phase of transmission coefficient as a function of the dc through the wire, $\Delta\phi(I)$, we extended the setup by adding a reference circuit. This mainly consists of a directional coupler inserted between the microwave source and the microwave switch, a calibrated variable phase shifter, and a T-connector inserted between the output transducer and the microwave detector. The directional coupler couples a small portion of the incident microwave power out of the main circuit. The power passes through a calibrated variable phase shifter and a variable attenuator. The T-connector feeds the power back into the main circuit, resulting in an interference of the output signal with the reference signal at the detector input. Variation of the dc through the wire produces a change of amplitude of the interference signal. To measure $\Delta\phi(I)$, one adjusts the inserted phase via the calibrated variable phase shifter to retrieve the same interference pattern as for I=0. For simplicity, we chose the destructive interference pattern as the pattern to retrieve. It corresponds to the minimum of the signal from the output antenna. The minimum in the dependence of the output signal on the inserted phase was easy to find in our experimental conditions. It was sharp enough to make reliable measurements.

The transmission characteristic measured applying a cw microwave signal to the input transducer of the structure is shown in Fig. 2. As one sees in the figure, the measured characteristic is typical for a BVMSW configuration. The maximum of transmission corresponds to the upper edge of the spin wave band and the transmission loss increases as the frequency is decreased. One also sees a small oscillation of the intensity of the transmitted signal with frequency. This oscillation is due to an interference of the spin wave signal received by the output antenna with the signal produced by direct microwave coupling of the structure's transducers.

To make measurements of the spin wave transmission through the inhomogeneity, we used a pulsed technique. Examples of profiles of detected output pulses are shown in the right panels of Fig. 2. Experimentally measured spin wave delay time on the path from the input to the output transducer was 320 ns. The half-time of the delay is the spin wave propagation time between the central conductor and the output or the input transducer. Output pulses longer than 320 ns show periodic variation of amplitude in their leading part when the carrier frequency is gradually changed. An example is the drop of intensity 320 ns before the trailing edge of the pulse in the upper panel of Fig. 3. This periodic variation is caused by beating at the output transducer of the spin wave pulse with a signal produced by direct microwave coupling of the input and the output transducers.

Pulses 170–320 ns in length also show a frequency variation of amplitude at their leading part. This variation is considerably weaker than that of the longer pulses. Since this effect disappears for $\tau \leqslant 170$ ns, we infer that the beat signal is also produced by interference at the output transducer of two pulses. There are two possible reasons for this. First is interference of the spin wave signal pulse with a pulse produced by direct microwave coupling of the central conductor with the output transducer. The central conductor may serve

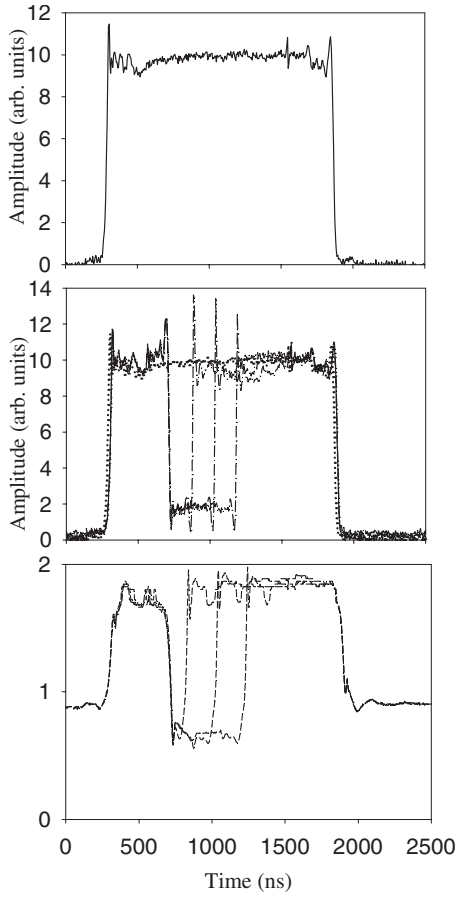

FIG. 3. Pulse profiles from the output transducer. Upper panel: No dc applied to the central conductor ($I=0$). Middle panel: Pulses of different lengths are applied: 100, 300, and 500 ns. Current strength is 0.5 A. Lower panel: Interference patterns of the output spin wave pulse with the reference signal (used for phase measurements) for the same lengths of dc pulses as in the middle panel. Input microwave pulses are 1600 ns long. The dotted line shows the interference pattern without dc applied.

as a "parasitic" receiving transducer for the spin wave pulse launched by the input transducer. If so, the microwave current induced in the central conductor is able to couple to the output transducer through its evanescent microwave field. Another possibility is that the signal produced by direct coupling of the input transducer to the central conductor excites a parasitic spin wave signal under the central conductor which arrives with a 170 ns delay to the output transducer. The beat signal produced by the spin wave pulse with this parasitic spin wave signal at the output transducer is received by the output transducer. Since the observed amplitude of beating is small, the efficiency of parasitic spin wave excitation and reception by the central conductor is also small compared with the amplitude of the main spin wave signal.

A small but abrupt drop in the *power* (intensity) of the output signal is visible at the half-width of the pulse in the upper right-hand panel of Fig. 2. The drop is due to beating as described above. The change in power level is less than 15%. The *amplitude* of the microwave field of the output signal changes considerably less; the drop in amplitude is only 7%. Furthermore, this drop vanishes for some value of the phase difference between the spin wave and the parasitic signals. For the measurements, we used the external field (H_s) values for which this drop vanishes.

Dispersion effects appear to have less impact on the measurement results. To illustrate this, in Fig. 3 we show the amplitudes of the output signals for long input pulses. Intentionally, the beginning of the current pulse was delayed by 400 ns with respect to the arrival of the leading edge of the spin wave pulse to the central conductor. As one sees in the upper panel, at these times the output pulse profile is flat if no current is applied to the central conductor. It is flat because at these times, the output transducer receives the central parts of both spin wave output pulse and the direct microwave coupling pulse. Both are smooth; therefore, the beating pattern of these two signals is independent of time.

The lower panel shows the output profiles for different lengths of the dc pulses. As one sees in the figure, the signal power quickly drops after application of the current and remains practically constant while dc is flowing through the conductor. This panel clearly demonstrates that the dc pulses as short as 100–150 ns can be used for measurements of cw-type spin wave transmission through the inhomogeneity region.

Thus, using reasonably short pulses as microwave input signals and applying the current through the central conductor in the pulse regime does not lead to a considerable error because of dispersion effects. Furthermore, it eliminates the uncertainty in the output amplitude due to beating of the output spin wave signal with the signal produced by direct microwave coupling of the input and the output transducers.

Using the pulse regime has yet another important advantage. A significant dc through such a thin wire may result in significant heating of the wire and of the film near the wire. It is well known that the temperature dependence of yttrium iron garnet (YIG) saturation magnetization at room temperature is quite strong.[26] Account of this is necessary in order to correctly interpret experimental results. Therefore, in any experiment involving increased powers, precautions should be taken in order to exclude heating. In experiments on highly nonlinear spin waves,[27] strong signals are usually applied as short pulses with a small repetition rate. This allows one to efficiently control the average power transferred from spin waves to the film crystal lattice by varying the repetition rate. In this experiment, the main source of heat is the dc though the central conductor. Therefore, heating of the sample can be suppressed or at least considerably reduced, if the current is applied as short pulses. For this purpose, in our experiments the pulses were applied with a very small repetition rate of 1 ms.

For the phase measurements, we used the method of interference of the spin wave signal with a reference signal. The reference signal represents a kind of artificially introduced direct coupling of the input to the output transducers. It travels with practically the same group velocity as the signal of the direct parasitic transducer coupling discussed above. Therefore, this interference pattern should have the same properties. In particular, in order to have a time-independent profile of the interference pattern, one needs a long time overlap of the output pulses. In our measurement,

this is achieved using a cw reference signal. Furthermore, as the amplitude of the reference signal is usually much larger than that of the parasitic direct coupling of the input and the output transducers, the influence of the parasitic signal on the interference pattern can be neglected. One can then use longer pulses in order to minimize influence of the dispersion effects on the output phase profile.

The above consideration allowed us to choose the input pulses 420–1360 ns in length for the phase measurements. In Fig. 3, one sees that approximately 150 ns after turning on the current through the central conductor, the amplitude of the interference pattern attains a level constant throughout the remaining part of the current pulse.

These preliminary measurements allowed us to choose optimal values for lengths of the spin wave and dc pulses from the point of view of exclusion of parasitic thermal processes and minimization of distortion of spin wave pulses by dispersion effects. The optimal length for dc pulses was found to be 100 ns for the amplitude measurements and 300 ns for the phase measurements. Spin wave pulses with lengths of 320 and 1360 ns, respectively, should be used in combination with these dc pulses.

The available equipment does not allow detection of any spin wave pulse reflected from the central conductor. Such a pulse would travel back to the input microwave transducer. With our equipment, we are not able to use the input transducer as an emitter of strong incident spin wave pulses and a receiver of the weak reflected spin wave pulses. However, in order to estimate the reflection of spin waves from the central conductor, we made measurements using a time and space Brillouin light scattering (BLS) method.[27] These measurements showed no reflected signal from the central conductor when no dc was applied.

On the other hand, for $I \neq 0$, a spin wave pulse reflected from the central conductor was clearly seen in BLS profiles (to be published elsewhere). Its amplitude was consistent with the power conservation law. In the following, this fact allows us to measure the amplitude of the transmitted spin wave solely. The shape and the amplitude of the reflected pulse may be recovered from the shapes of the incident and transmitted signals, provided the spin wave damping rate for the film sample is known.

Results of our measurements are shown in Fig. 4. We found that in the tunneling regime, for negative I values the behavior of the amplitude of the complex transmission coefficient (shown in the upper panel of Fig. 4) is the same as that previously measured in Ref. 22 The amplitude of the transmitted signal decreases monotonically with $|I|$. This was explained in Ref. 22 as an increase of the length of the zone prohibited for BVMSW propagation with the increase of the current magnitude. The decrease of transmission is stronger for larger incident wave numbers.

The important result in this case is the phase characteristic. The characteristic is not linear as the phase demonstrates a tendency to saturate at large currents. Small phases are achieved by small incident wave numbers at constant current.

Measurements with a well generated by a positive current show that scattering of BVMSW packets results in a transmission amplitude that depends nonmonotonically on the magnitude of the dc. A pronounced minimum is seen at 0.5–0.6 A. The magnitude of transmission in this minimum increases with increasing k_0. A weak maximum appears at a current about 1 A. For smaller wave numbers of the incident wave (k_0=49–83 rad/cm), the transmission in the maximum is unity, whereas for larger wave numbers (k_0=116 and 158 rad/cm), the transmission at the maximum is only partial.

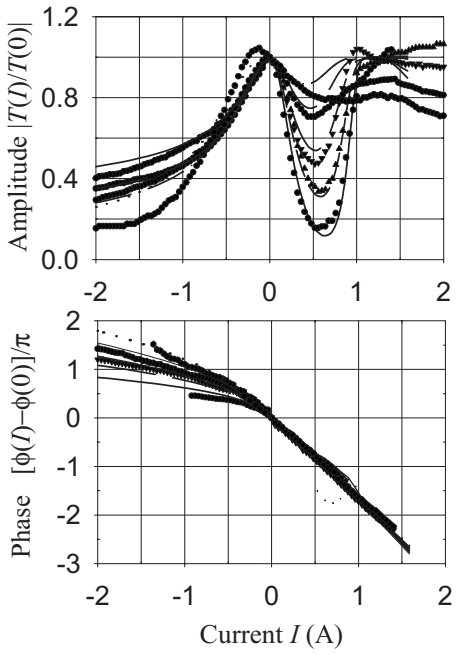

FIG. 4. Measured and calculated transmission coefficients. The upper panel shows the amplitude, whereas the lower panel shows the phase. Symbols show experimental data. Lines show results of numerical calculation. Measurements and calculations were made for k_0=49, 63, 83, 116, 158, and 267 rad/cm. Upper panel, $I>0$: The lowest curve corresponds to k_0=49 rad/cm, whereas the highest one to k_0=158 rad/cm. Upper panel, $I<0$: The curves (experimental and theoretical) showing the largest transmission at I=−2 A are for k_0=49 rad/cm, whereas those showing the lowest one are for k_0=267 rad/cm. The theoretical and the experimental lines for middle curves nearly coincide. Lower panel, $I>0$: All the curves practically coincide within the graphical accuracy. Lower panel, $I<0$: The lowest curves (experimental and theoretical) are for k_0=49 rad/cm, whereas the highest ones are for k_0=267 rad/cm. In order to achieve good agreement, the shown experimental values of positive currents were reduced to 88.1% of actually measured values.

The phase of the transmitted signal shown in the lower panel has a general tendency to decrease linearly with I, but with noticeable deviations from linearity in the vicinities of I values which correspond to the minimum and the maximum (on the right-hand side) in the upper figure. The depth of the minimum is inversely related to k_0 and corresponds to strongly nonlinear behavior of $\Delta\phi(I)$.

As one sees in Fig. 4, the results for phase at positive currents are shown only up to I=1.5 A. The reason for this is that the controllable phase shifter we used in our phase measurements was able to shift the phase of the microwave reference signal only up to 2.5π. For negative I values, this was

sufficient to cover the whole range of accessible dc values, but for the positive currents, we were obliged to stop our measurements at $I=1.5$ A because of the stronger slope of $\Delta\phi$ dependence on I. Similarly, we show the amplitude characteristic for the smallest value of k_0 only up to 1.5 A. We were not able to measure the amplitude for larger currents because of significant oscillations in the profile of the output pulse.

Note that the current of 1.5 A through the wire corresponds to an Oersted field of 240 Oe at the wire surface. The Oersted field in the center of the inhomogeneity region (Fig. 1) averaged across the film thickness is 200 Oe. Below, we will find that in order to get good agreement with the experiment, one needs to assume that the wire was located at a distance of 10 μm from the film surface. At that distance, this average field reduces to 120 Oe. The static field applied to the sample during the measurements was in the range 1813–1844 Oe. This field is much larger than the maximum Oersted field of the current through the wire.

Note that the measured phase characteristic allows one to independently check for the influence of Ohmic heating by the dc on the experimental results. As stated above, a local heating of the YIG film would locally reduce the film saturation magnetization, similar to the example shown in Fig. 1(b) for the negative Oersted field. A decrease of saturation magnetization should shift the dispersion curve downward, like the negative Oersted field does in Fig. 1(b), opposite to the shift induced by the actual positive Oersted field of the wire [shown in Fig. 1(c)]. The Oersted field is linearly proportional to the current, whereas the heat is proportional to I^2. Thus, a possibility exists that for larger positive I values, these local shifts of the dispersion curve compensate each other, which might result in full transmission at the point of full compensation. Therefore, one can suppose that the nonmonotonic behavior of the transmitted amplitude showing full transmission for $I=1$ A in Fig. 4 has the simple explanation that the maximum at 1 A is the point of the compensation. In such a case, the phase of the transmitted signal at the point of compensation would be close or equal to the value at $I=0$. Furthermore, the influence of the Oersted field should dominate the thermal effects at smaller currents. In the range 0.5–1 A, the entire phase characteristic would be strongly nonmonotonic with a minimum situated at the same point as for the amplitude (Fig. 4, upper panel). Since the measured phase characteristics are instead linear, this explanation cannot account for the observed nonmonotonic behavior of the amplitude.

II. THEORY

We now construct a theory able to explain the observed amplitudes. The theory is also able to explain the measured nonlinear phase dependence on I in the tunneling regime ($I<0$).

The propagation of dipolar spin waves in a film geometry is complicated because of off-diagonal terms in the permeability associated with the gyromagnetic response. However, for the special case of a plane wave traveling in the z direction (BVMSW) and incident normally on a discontinuity with translational invariance in the xy plane, the off-diagonal terms are not important and the wave satisfies the integral equation

$$\chi(z,\omega)^{-1}m_x(z) - \int_{-\infty}^{+\infty} 4\pi G_{xx}(z,z')m_x(z')dz' = A\,\delta(z-z_0). \tag{1}$$

Here, $\chi(z,\omega)$ is the diagonal term of the microwave magnetic susceptibility tensor $\hat{\boldsymbol{\chi}}$ (Ref. 28 and 29) and z is the direction of BVMSW propagation. The kernel $4\pi G_{xx}(z,z')$ is the out-of-plane diagonal component of an approximate quasi-1D Green's function $\mathbf{G}(z,z\prime)$ for the magnetostatic field produced by sources in a planar geometry. The Green's function was first obtained in Ref. 30 and the diagonal out-of-plane component has the form

$$4\pi G_{xx}(z,z') = \frac{2}{L}\ln\frac{(z-z')^2}{L^2+(z-z')^2}, \tag{2}$$

where L is the film thickness. The Dirac delta function in Eq. (1) describes the linear excitation of an incident monochromatic spin wave by a source at a point z_0 located far from the inhomogeneity ($z_0\to-\infty$). A is the excitation amplitude of the source. A derivation of Eq. (1) is given in Appendix A.

Propagating dipole-dominated BVMSWs exist in the range $-1<\chi(z,\omega)^{-1}<0$ (see, e.g., Refs. 25 and 29). Outside this range, only evanescent waves can exist.[22] In the experimental situation, $\hat{\boldsymbol{\chi}}(\omega,z)$ depends on position z because of the spatial variation of the field inhomogeneity. The total static magnetic field is a superposition of the applied field $\mathbf{H}_s=H_s\mathbf{e}_z$ and $\delta\mathbf{H}(z)$, the field created by the dc in the neighboring wire. For simplicity, we consider only the in-plane component of this field so that the total field is entirely along the z direction with magnitude $H(z)=H_s+\delta H_z(z)$. Far from the wire, the field is due only to H_s so that $H(z\to\pm\infty)=H_s$.

The value of the z component of the wire induced field averaged through the film thickness is

$$\delta H_z(z) = Y(z)I, \tag{3}$$

where $Y(z)$ is the profile of the field created by the current. One can show that for cylindrical wire,

$$Y(z) = \frac{1}{5L}\ln\frac{z^2+(r+d+L)^2}{z^2+(r+d)^2}, \tag{4}$$

where I is the dc, r is the wire radius, and d is the nearest distance between the surfaces of the wire and the film.

A. Numerical solution of the equations of motion

First, we solve Eq. (1) numerically. Because in the experiment spin waves are not monochromatic, we first generalize Eq. (1) as an inhomogeneous time-dependent integrodifferential equation. This allows us to make calculations for pulsed spin wave propagation.

We make calculations for incident spin wave pulses 100–300 ns of duration and register the amplitudes of transmitted signals in the center of the pulses. Our first main observation is that the amplitudes of the transmitted and re-

flected pulses of such length far away from the pulse edges do not depend on the pulse duration; thus, in the later analytical treatment, for the sake of simplicity we may consider monochromatic spin waves.

The solid lines in Fig. 4 show the results of the numerical solution. As in the experiment, amplitudes and phase from the center of pulses are shown. As seen in the figure, there is good agreement between the simulation and experiment. A free parameter used for the fit was spacing, taken as $d=10$ μm [Eq. (4)] between the wire and the film surface.

In order to achieve good agreement, the shown experimental values of positive currents were reduced to 88.1% of actually measured values. Reasons for the reduction include neglect of the out-of-plane component of the current created field $\delta H_x(z)$ and use of a one-dimensional Green's function of the dipole field $G_{xx'}(z,z')$. These two factors should increase the reflection from the inhomogeneity, and thereby enhance the effect of I on transmission. The reduction may also describe the influence of residual heating effects. As a result, our numerical treatment probably underestimates the current.

Despite underestimating the current, the model of Eq. (1) is able to describe the main effects observed in the experiment. Calculation of power carried by pulses shows that the sum of powers carried by the transmitted and reflected pulses is equal to the difference of the power of the input spin wave pulse and the power lost due to magnetic damping. Energy is conserved and we can conclude that the minimum of propagation in the calculated dependences corresponds to the maximum of reflection.

Finally, we note that the numerical solution of the time-independent Eq. (1) introduces spurious full reflection from the integration boundaries. The time-dependent equation for pulses we used allows us to separate the transmitted and the reflected pulses through time delays. We can therefore identify unambiguously transmitted and reflected power without significant losses to spurious reflections.

B. Integral equation formulation of the scattering problem

Additional insight into the problem is obtained using an alternative solution method.

We consider monochromatic spin waves and assume that $\delta H_z(z) \ll H_s$. This allows us to transform Eq. (1) into

$$m(z) = I\int_{-w/2}^{w/2} G_{exc}(z,z')\,\delta\upsilon(z',\omega)m(z')dz' + \exp(ik_0^c z). \tag{5}$$

The derivation of Eq. (5) is shown in Appendix B. In this equation, $I\delta\upsilon(z,\omega)=[\chi(z,\omega)^{-1}-\chi(z=\pm\infty,\omega)^{-1}]/(4\pi)-[O(I/Hs)^2]$, k_0^c is the complex wave number of the incident spin wave, and $-w/2<z<w/2$ is the region of localization of the current created field. An expression for G_{exc} is given in Eq. (B16) and determined from Eq. (B7). A key point for our analysis is that the finite range of integration in Eq. (5) results in a discrete spectrum of eigenmodes.

Equation (5) for the spin wave amplitude is now analogous to the Green's function formulation of the direct scattering problem in quantum mechanics (see, e.g., Ref. 31), and $I\delta\upsilon(z,\omega)$ plays the role of a scattering potential.

C. Green's function and Born approximation

Equation (5) represents a sum of the incident and scattered fields of the form $m(z)=S(z)+\exp(ik_0^c z)$, where the scattered field $S(z)$ is the integral $S(z)=I\int_{-w/2}^{w/2}G_{exc}(z,z')\,\delta\upsilon(z',\omega)m(z')dz'$. Far away from the inhomogeneity, the scattered field can be decomposed into a sum of two waves: $S(z)=S_+(z)+r(z)$, where $S_+(z)$ is the forward scattered wave and $r(z)$ is the backscattered (reflected) wave.

Later, we will solve Eq. (5) exactly, but some insight can be gained by using Born's approximation.[31] In the first Born's approximation to obtain amplitudes of the transmitted, reflected, and scattered waves, it is necessary to place the observation points far away from the inhomogeneity. This reduces the Green's function to a simple expression [Eq. (B18)]. The scattered field approximated to first order is found by calculating $S(z)$ using $m(z)=\exp(ik_0 z)$. Neglecting spin wave losses by setting $\upsilon_0''=0$ (see Appendix B for the definition of the loss parameter υ_0''), the transmitted and reflected amplitudes in the first Born approximation far from the scattering inhomogeneity are

$$S_+(z) = i\frac{2I}{L}\exp(i|k_0|z)\int_{-w/2}^{w/2}\delta\upsilon(z',\omega)dz', \quad z \gg w/2,$$

$$r(z) = i\frac{2I}{L}\exp(-i|k_0|z)\int_{-w/2}^{w/2}\delta\upsilon(z',\omega)\exp(2i|k_0|z)dz', \quad z \ll w/2. \tag{6}$$

The amplitude of the transmitted wave $S_+(z)$ is linearly proportional to the area of the inhomogeneity profile $\Xi=\int_{-w/2}^{w/2}\delta\upsilon(z',\omega)dz'$. This quantity is the zeroth order spatial Fourier component of the inhomogeneity profile. The reflection amplitude is proportional to the $2k_0$ Fourier component of the inhomogeneity profile: $Q=\int_{-w/2}^{w/2}\delta\upsilon(z',\omega)\exp(-2i|k_0|z)dz'$, i.e., the first resonant Bragg backscattered wave.

Both integrals for the inhomogeneity profile can be calculated. Using the notation in Appendix B, the results are

$$\Xi = \frac{2}{5}\pi\eta(\omega),$$

$$Q = \frac{2}{5}\pi\eta(\omega)[1-\exp(-2|k_0|L)]\exp[-2|k_0|(r+d)]/[2|k_0|L]. \tag{7}$$

The transmission coefficient is $|T|=|S_+(z)+\exp(ik_0 z)|=\sqrt{1+(2I\Xi/L)^2}$. For $I\neq 0$, we have the unphysical result that $|T|>1$ and the first Born approximation clearly fails even for small I. Nevertheless, examination of the upper panel in Fig. 5(b) shows that the first order Born approximation estimates $|S_+(z)|$ well for small I. The problem with the transmitted coefficient T is because of the incorrect treatment of the

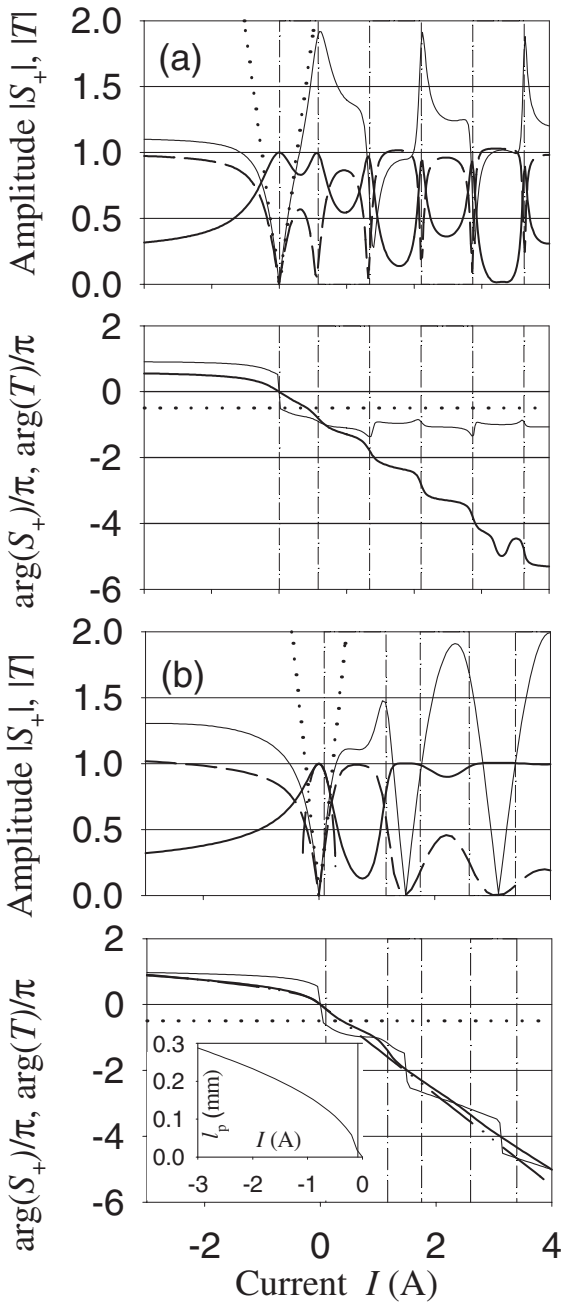

FIG. 5. Amplitudes (upper panels) and phases (lower panels), of transmitted (solid line), reflected (dashed line), and scattered (thin solid line) waves (a) for a rectangular-shaped inhomogeneity and (b) for the wire with current. For comparison, the dotted lines show the amplitude and phase of the forward scattered wave calculated in the first Born approximation, and the dash-dot-dotted line in the lower panel of (b) is the WKB approximation for the phase of transmission coefficient. The dash-dot-dotted line in the upper panel of (b) is the transmission coefficient calculated as $|T|=\sqrt{1^2-|R|^2}$ with R from the first Born approximation. Thin vertical dash-dotted lines show the positions of the transmission resonances, as calculated from Eq. (8) for these potential shapes. The inset in the lower panel of (b) shows the dependence of the length of prohibited zone on the wire current.

phase of $S_+(z)$. This is illustrated in the lower panel of Fig. 5(b).

For $|k_0|L \ll 1$, the quantity $[1-\exp(-2|k_0|L)]/(2|k_0|L)$ appearing in $r(z)$ reduces to $1-2|k_0|L$. Hence, Q is an increasing function of I and a decreasing function of k_0 and approaches zero as $k_0 \to \infty$. If there is no dissipation, we require $|T|=\sqrt{1^2-|R|^2}$. Hence, the transmission coefficient decreases with $|I|$ and increases with increasing k_0. This behavior is in qualitative agreement with experiment and also with results from the more rigorous solution of Eq. (5) as depicted in Fig. 5(b). Note that the range of validity is $|I| \leq L/(2Q)$, where the reflection coefficient remains less than 1. Furthermore, the experiment is able to probe the range from $k_0=0$ to $k_0=200$ rad/cm, which means that our Born approximation is valid only for currents less than 0.38 A at most. This is a much smaller range than accessible in existing experiments.

D. Exact solution to the integral equation

The difficulty with a perturbative approach is its inadequacy of describing the near field. In Fig. 4, we see that a good approximation for T will require at least a third order dependence on I, and therefore will require several terms beyond the leading one in a perturbation expansion. This is cumbersome, as one needs to use the whole Green's function for substitution into higher-order term integrals. We use instead a different method based on an eigenfunction expansion of the integral operator kernel in Eq. (5).

We first solve

$$\lambda u(z) = \int_{-w/2}^{w/2} G_{exc}(z,z')\,\delta\upsilon(z',\omega)u(z')dz', \tag{8}$$

and the transposed operator

$$\lambda \phi(z) = \delta\upsilon(z,\omega)\int_{-w/2}^{w/2} G_{exc}(z',z)\,\phi(z')dz' \tag{9}$$

for eigenfunctions and eigenvalues. Note that with the substitutions $u(z)=\tilde{u}(z)/\sqrt{\delta\upsilon(z,\omega)}$ and $\phi(z)=\sqrt{\delta\upsilon(z,\omega)}\tilde{\phi}(z)$, both equations are seen to have the symmetric kernel $\sqrt{\delta\upsilon(z,\omega)}G_{exc}(z,z')\sqrt{\delta\upsilon(z',\omega)}$.

Once the eigenvalues and the eigenfunctions are found, the solution of the inhomogeneous equation is expressed as follows:

$$m(z) = m_{exc}(z), \tag{10}$$

where

$$m_{exc}(z) = \sum_{n=0}^{\infty} \frac{\int_{-w/2}^{w/2} \exp(ik_0^c z')\,\phi_n(z')dz'}{1-I\lambda_n} u_n(z). \tag{11}$$

To obtain Eq. (11), we use the biorthogonality of the sets of eigenfunctions

$$\int_{-w/2}^{w/2} \phi_n(z)u_{n'}(z)dz = N_n^2\delta_{nn'}, \tag{12}$$

and normalize the functions such as $N_n=1$. Solution (10) is valid inside the interval of the biorthogonality of the func-

tions $u(z)$ and $\phi(z)$: $-w/2<z<w/2$ [Eq. (12)]. As seen from Eq. (11), $m(z)$ may depend on I in a resonant way. The resonant condition is

$$\mathrm{Re}(1/\lambda_n) - I = 0. \tag{13}$$

The scattered field is then the difference between the full solution [Eq. (10)] and the unscattered wave:

$$S(z) = m_{exc}(z) - \exp(ik_0^c z), \quad -w/2 < z < w/2. \tag{14}$$

In the vicinity of the incidence boundary of the inhomogeneity near $z=-w/2$, the scattered field represents only a reflected wave. Hence, the solution for the reflected wave is

$$r(z) = m_{exc}(z) - \exp(ik_0^c z), \quad -w/2 < z \ll 0. \tag{15}$$

Similarly, near $z=w/2$, only the unscattered and the forward scattered waves are present. Here, the solution for the transmitted wave is

$$t(z) = S(z) + \exp(ik_0^c z) = m_{exc}(z), \quad 0 \ll z < w/2. \tag{16}$$

As stated above, the solutions in Eqs. (14)–(16) are valid only inside the inhomogeneity. An expression valid at any z is obtained by substituting Eq. (10) into Eq. (5). The scattered field is then

$$S(z) = I\int_{-w/2}^{w/2} G_{exc}(z,z')\,\delta v(z',\omega) m_{exc}(z')dz', \quad -\infty < z < \infty. \tag{17}$$

Furthermore,

$$r(z) = S(z), \quad z < -w/2 \tag{18}$$

and

$$t(z) = S(z) + \exp(ik_0^c z), \quad z > w/2, \tag{19}$$

with $S(z)$ from Eq. (17).

The transmission coefficients R and T are found by the asymptotic limit $z \ll w/2$ of Eq. (18) and $z \gg w/2$ of Eq. (19). In what follows, we find the eigenfunctions $u(z)$ and $\phi(z)$ numerically on the finite interval $-w/2<z<w/2$.

We note that in the limiting case $w\to\infty$ [which corresponds to a smooth potential like Eq. (4)], the biorthogonality interval is the whole z axis and one should use Eqs. (15) and (16), rather than Eqs. (18) and (19) to calculate T and R. In this limit, $|R|=|r(-w/2)|$ and $|T|=|t(w/2)|$.

In Appendix C, we derive an explicit formula having a validity range larger than that obtained in Born's approximation and free of necessity to numerically solve the eigenvalue problem [Eqs. (8) and (9)].

III. DISCUSSION

In the numerical implementation of the eigenfunction method described above, care must be taken with the finite width of the inhomogeneous region. At the boundaries of the inhomogeneity, $\delta v(z,\omega)$ discontinuously changes to zero. A nonphysical reflection from the boundary will appear but can be minimized by decreasing the magnitude of the jump. This is accomplished by choosing a large w in Eq. (5). Since the current induced field of the thin wire is highly localized, it is not difficult to satisfy this condition in numerical calculations.

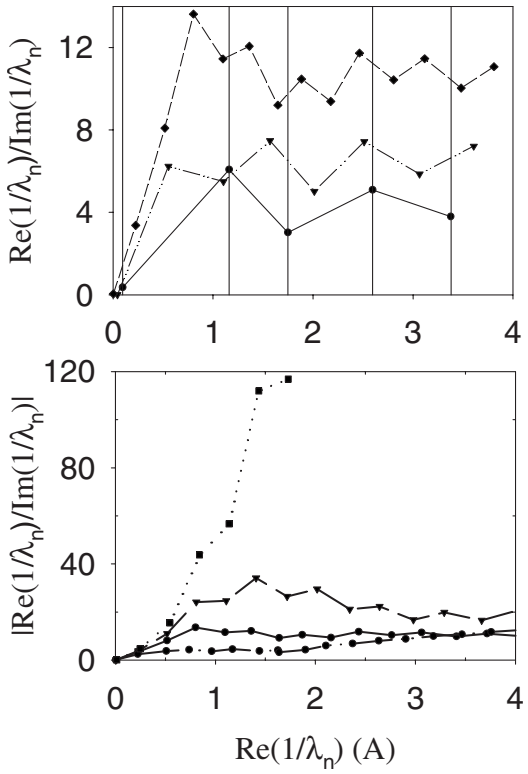

FIG. 6. Complex eigenvalues λ_n of Eqs. (8) and (9) shown as "quality factors" $\mathrm{Re}(1/\lambda_n)/\mathrm{Im}(1/\lambda_n)$ vs real eigenvalue parts $\mathrm{Re}(1/\lambda_n)$. Upper panel: The solid line is for the experimental profile (4) [in terms of Eq. (21), $t=50$ μm, $l_{eff}=25$ μm]. The dashed and the dash-dotted lines are for the profile (21) of lengths $t=200$ and 100 μm, micrometers respectively. Lower panel: The same for the profile (21) but with different steepness of the edges. The solid line is for the experimental edge steepness $l_{eff}=25$ μm, whereas the dashed and the dash-dotted lines are for the edges with the effective lengths of 15 and 50 μm. The dotted line is for the square-shaped inhomogeneity [Eq. (20)]. The whole length of the inhomogeneity t in the lower panel is 200 μm.

The solid line in the upper panel of Fig. 6 is the result from a calculation of the eigenvalues of Eqs. (8) and (9). For this calculation, $w/2$ was set equal to $80r$. This corresponds to a jump in the inhomogeneity field $\delta\mathbf{H}(w/2)=6\times10^{-4}$ $\delta\mathbf{H}(0)$. Such a small jump of the field does not produce any noticeable reflections in the simulation. In the experiment, the strength of dc applied current did not exceed ±2 A, so by the resonant condition in Eq. (13), the relevant inverse eigenvalues are small: $-5\ \mathrm{A}<\mathrm{Re}(1/\lambda_n)<5\ \mathrm{A}$ in this particular case.

The eigenvalues belonging to this range are situated in the complex plane close to the real axis. As a rule, the real parts are larger than the imaginary parts. As seen in Fig. 6, the inverse eigenvalues are not distributed evenly along the real axis and the distance between neighboring points on the real axis changes nonmonotonically with frequency.

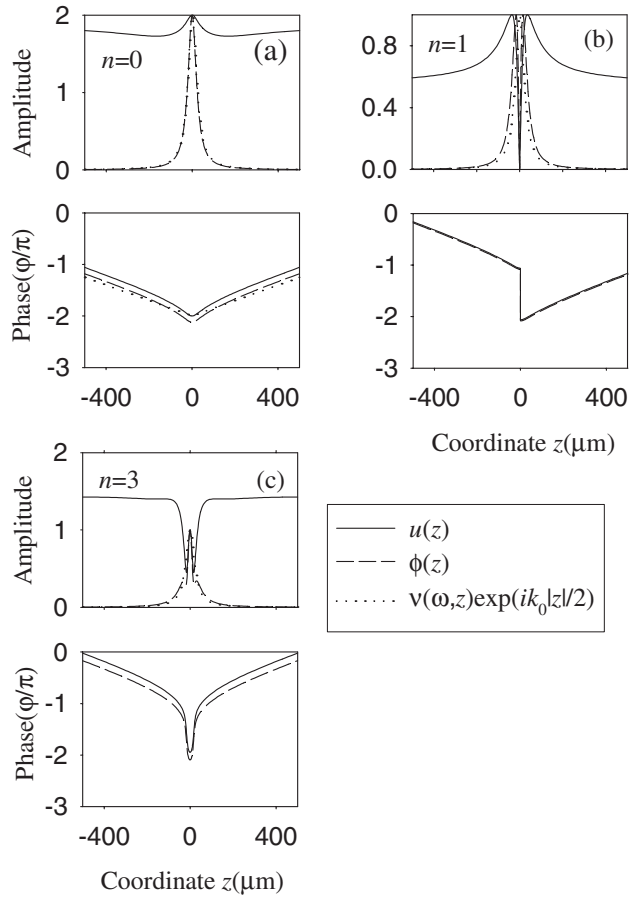

FIG. 7. Lowest eigenfunctions of Eqs. (8) and (9) for $k_0=47$ rad/cm. (a) $n=0$ $(1/\lambda_0=0.098-0.279i)$, (b) $n=1$ $(1/\lambda_1=1.193-0.1198i)$, and (c) $n=2$ $(1/\lambda_2=1.172-0.597i)$. The upper panels are amplitudes of the complex eigenfunctions, and the lower panels are their phases. Solid lines show eigenfunctions of Eq. (8), and the dashed lines those of the transposed problem [Eq. (9)]. The dotted lines show the profile of the Oersted field [Eq. (4)] and the linear phase profile $\exp(ik_0|z|)$.

In Fig. 7, the calculated eigenfunctions of Eqs. (8) and (9) are shown. The eigenfunctions of the transposed operator [Eq. (9)] determine the scattering efficiency since they determine the overlap integral with the incident wave in the numerator of Eq. (11). These modes are localized at the inhomogeneity and the modulus of the lowest frequency mode is very close to the profile of the inhomogeneity field given by Eq. (4). The eigenfunctions of Eq. (8) determine the amplitude of the scattered waves at $z=\pm\infty$, and hence represent the reflection and transmissions coefficients. These functions have the asymptotic form of monochromatic traveling waves at $z=\pm\infty$.

The transmission coefficient calculated from Eqs. (11) and (16) with the eigenfunctions shown in Fig. 7 is presented in Fig. 8. Experimental data and the results of numerical simulation from Fig. 4 are shown for comparison. There is good agreement with the experiment for both calculations. The small discrepancy between the numerical simulation and the eigenfunction expansion results is due to keeping only the first two terms in k_0 in the expansion of $W(k)$ [Eq. (B15)] and only the first two terms in I in the expansion of the inhomogeneity profile [Eq. (5)].

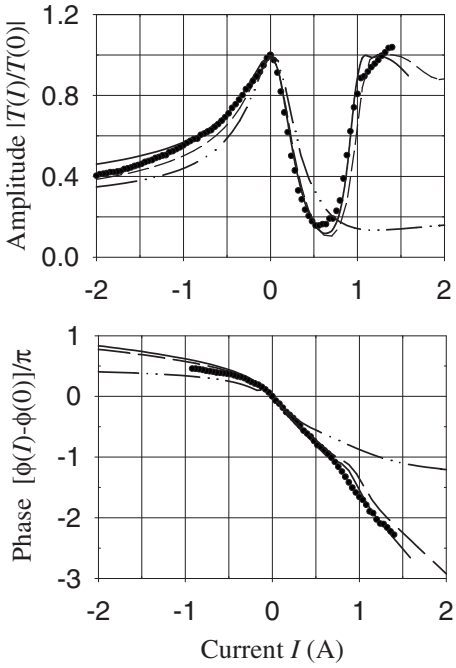

FIG. 8. Transmission coefficient. Upper panel, Amplitude; lower panel, phase. Solid line, numerical calculation; dashed line, approximate analytical calculation; dash-dot-dotted line, approximated calculation by using Eq. (B19); symbols, experiment. Initial wave number $k_0=47$ rad/cm.

The profiles of the amplitude and phase of the transmitted wave given by Eq. (16) are shown in Fig. 5(b). The reflected wave from Eq. (15) and the forward scattered wave from Eq. (14) are also shown. The calculation is made over a large range of I values in order to assess the validity of the approximations made using Eqs. (B1) and (B15).

One sees in Fig. 5(b) that minima observed in the experimentally accessible range of small I values are not unique. Weaker minima appear for larger values of I as well. Vertical lines in the figure show the positions of roots of Eq. (13). The roots do not fully coincide with the positions of transmission maxima. Except the trivial root $n=0$ at $I\approx 0$, the next roots are situated at the edges of wide plateaus of full transmission.

A. Transmission resonances for a rectangular inhomogeneity

We can identify the origin of the plateaus by solving Eq. (5) for the case of the rectangular-shaped inhomogeneity modeled by the expression below:

$$\delta\upsilon(z,\omega)=\begin{cases}\delta\upsilon(0,\omega), & -w/2<z<w/2\\ 0, & z<-w/2, z>w/2,\end{cases} \tag{20}$$

where $\delta\upsilon(0,\omega)$ is $\delta\upsilon(z,\omega)$ from Eq. (B3) with Eq. (4) calculated by setting $z=0$. With this profile, the integral operator in Eq. (5) with Eq. (20) reduces to an integration of $G_{exc}(z,z')$ over $-w/2<z'<w/2$. In order to make the phenomenon more pronounced, we set the length of the rectan-

gular inhomogeneity greater than the actual wire diameter and use a large incident wave number: $w=100$ μm with $k_0=120$ rad/cm. The inhomogeneity profile of Eq. (20) describes the magnetic field created by a dc through a thin stripe conductor placed directly on the film surface.

The panels in Fig. 5(a) contain the solution of Eq. (5) for this rectangular-shaped inhomogeneity. As seen in the upper panel, scattering of BVMSW results in a set of distinct maxima in $|T(I)|$ and $|S_+(I)|$ for $I>0$. Positions of the maxima coincide with the roots of Eq. (13). It indicates that these are indeed resonances. Since Eq. (11) is the scattering problem, we may infer that these are "transmission resonances."

Transmission resonances are created by multiple reflections from the inhomogeneity boundaries and occur when an incident wave excites unstable bound states. A transmission resonance occurs when the wave reflected from the boundaries inside the inhomogeneity interferes constructively with the incoming wave. Destructive interface leads instead to enhanced reflection.

There are similarities between the above transmission resonances and the quantum mechanical problem of scattering from a one-dimensional potential well. The difference is that in the present case, we cannot write the scattered spin waves as simple plane harmonic waves because of the nonlocality of the dipole interaction. The dipole interaction couples the sources inside and outside the inhomogeneity so that purely propagating harmonic solutions with k_0 and k_i exist only far away from the boundaries. This means that boundary scattering involves a superposition of all modes and cannot be simplified at each interface into scattering between three waves as in the one-dimensional quantum well problem.

In the case of rectangular inhomogeneity, it is easy to analyze the transmission in terms of partial reflection of waves from the inhomogeneity boundaries. The first minimum of transmission coincides with the fist maximum of reflection [dashed line in Fig. 5(a)] when the partial waves reflected from the front and the rear boundaries are in phase. The maximum transmission takes place when these partial waves cancel each other at the front boundary. Since the wave inside the inhomogeneity may be reflected several times from the boundaries, this forms a transmission or reflection resonance.

To gain more insight into formation of resonances, we made additional numerical calculations for spin wave propagation through the rectangular inhomogeneity in the pulse regime using the same method as in Sec. II. The length of the inhomogeneity was chosen to be as long as possible (several millimeters). The phases of spin wave pulses reflected from the front edge of the inhomogeneity for $I>0$ (reflection from a positive step on the static-field profile) and for $I<0$ (reflection from the negative step) were calculated. We found that the phase of the reflected pulse is shifted by π with respect to the incident wave if $I>0$. The phase difference is zero if $I<0$.

The latter case models well the reflection from the rear boundary of short positive ($I>0$) rectangular inhomogeneity in Fig. 5. The numerical calculations show that the minima of transmission correspond to a phase accumulation of an odd multiple of $\pi/2$ by the wave propagating in the forward direction inside the inhomogeneity. The wave accumulates this phase as it travels from the front boundary to the rear boundary. The wave reflected from the rear boundary accumulates the same phase on its way to the front boundary, since the internal reflection from the rear boundary results in no phase shift, as discussed before. Consequently, the phase accumulated along the whole loop is an odd number of π, and the signal that passed along the whole loop meets the wave reflected back from the front boundary with the phase difference equal to an even number of π.

Similarly, in the maxima of transmission, the phase accumulated on the length of the inhomogeneity is equal to an even number of π. Consequently, the partial wave going directly through it meets in phase the wave reflected first from the rear boundary and then from the front one.

By way of an optical analogy, a region of increased magnetic field acts as a region of increased refraction index for BVMSWs. This analogy does not go far, however. Because of strong near fields at the boundaries due to the long-range dipole interaction, a standing wave profile with a definite value of k_i exists only far away from the boundaries of the inhomogeneity. This precludes, for example, the use of transfer matrices for formulating the problem.

B. Transmission resonances with a smooth profile inhomogeneity

Scattering resonances are not formed at all for some kinds of smooth potentials[32] and, in general, the problem can be complicated. In order to gain insight into the effect of the inhomogeneity profile on scattering, we have solved Eq. (5) for a modified rectangular inhomogeneity profile:

$$\delta v(z,\omega)=\begin{cases}\delta v(z+t/2-l_{eff},\omega), & z<-t/2+l_{eff}\\ \delta v(0,\omega), & -t/2+l_{eff}\leqslant z\leqslant t/2-l_{eff}\\ \delta v(z-t/2+l_{eff},\omega), & z>t/2-l_{eff},\end{cases} \tag{21}$$

where $\delta v(z+t/2-l_{eff},\omega)$ and $\delta v(z-t/2+l_{eff},\omega)$ are $\delta v(z,\omega)$ from Eq. (B3) calculated by setting $z=z+t/2-l_{eff}$ or $z=z-t/2+l_{eff}$ in Eq. (4), respectively.

This profile has smooth boundary slopes and a plateau of constant amplitude $\delta v(0,\omega)$ of length $t-2l_{eff}$. The length of each slope measured at midheight is equal to $l_{eff}=\sqrt{(r+d_0)(r+d_0+L)}$. The entire length of the inhomogeneity from these points is t. A finite spacing of $d=10$ μm between the wire and the film surface is again used, giving a length of $l_{eff}=25$ μm for a wire diameter of 25 μm.

Calculations were made for $t=200$, 100, and 50 μm. Results are shown in Fig. 9. $|T(I)|$ exhibits a set of maxima for positive I for the longest t. The positions of maxima coincide with the roots of Eq. (13) as expected. The positions of each second resonance for $t=200$ μm almost coincide with the positions of resonances for $t=100$ μm. At large I, plateaus of perfect transmission are formed instead of the peaks. The reason is that roots of Eq. (13) are situated in this case very close to each other.

The calculation using the experimental inhomogeneity profile of Eq. (4) is shown in the lower panel of Fig. 9. The

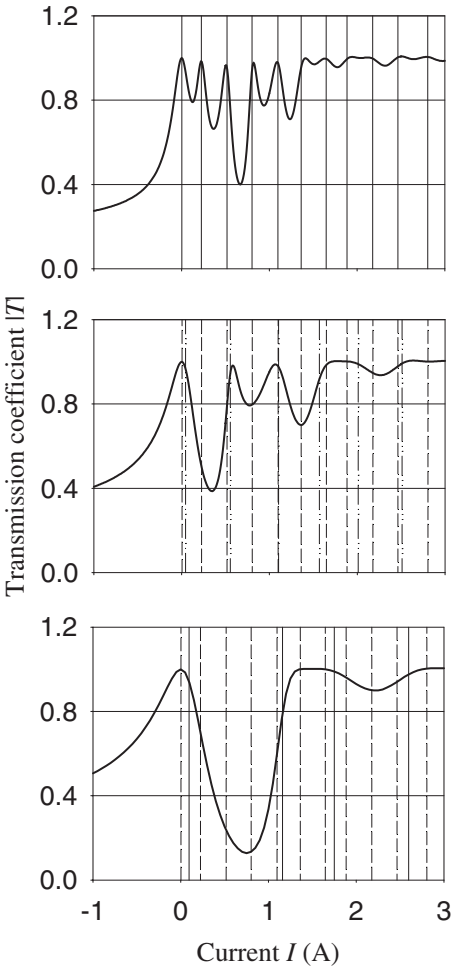

FIG. 9. Transmission coefficient vs dc magnitude for the inhomogeneity profiles (21). Lower panel: Experimental inhomogeneity profile (4) ($t=50$ μm, $l_{eff}=25$ μm). Middle panel: $t=100$ μm, $l_{eff}=25$ μm. Upper panel: $t=200$ μm, $l_{\mathrm{eff}}=25$ μm. Thin lines show positions of roots of Eq. (13). Dashed line: For the largest inhomogeneity $t=200$ μm, $l_{eff}=25$ μm. Dash-dotted line $t=200$ μm, $l_{eff}=25$ μm. Solid line: $t=50$ μm, $l_{eff}=25$ μm. For convenience of comparison, the dashed line is shown in all the panels.

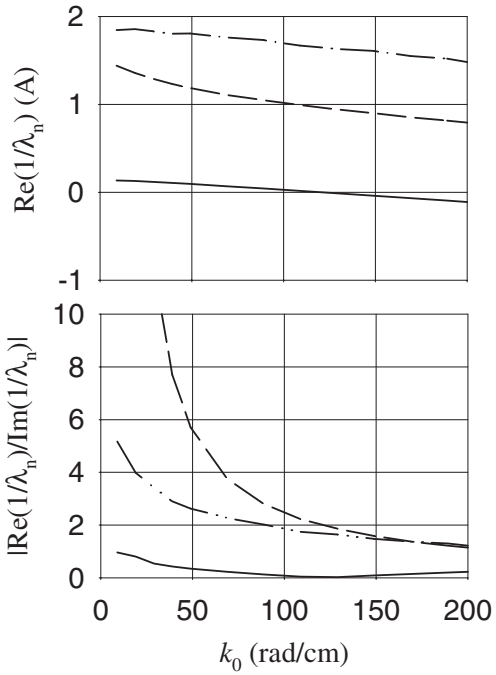

FIG. 10. Real parts of inverse eigenvalues (upper panel) and the "quality factors" for eigenvalues (lower panel) vs the incident wave number k_0. Solid line: The trivial eigenvalue $n=0$. Dashed line: $n=1$. Dash-dotted line: $n=2$.

positions of the roots of Eq. (13) nearly coincide with each fourth root for $t=200$ μm, and each second root for $t=100$ μm. No sharp resonance is visible and only plateaus of perfect transmission are formed. As seen in the upper panel of Fig. 6, the inverse eigenvalues are closely spaced for these currents. The values $\mathrm{Im}(1/\lambda_n)$ determine the width of resonance lines, and the plateaus are formed by overlapping of neighboring resonances because of large resonance linewidths.

The quality factor of the resonances is $\mathrm{Re}(1/\lambda_n)/\mathrm{Im}(1/\lambda_n)$ and decreases with the length of the inhomogeneity. A linewidth of a loaded resonance is proportional to the coefficient of coupling of the resonator to the external waveguide and inversely proportional to the energy stored in it. In our case, the coupling depends on the reflection coefficient of the inhomogeneity boundaries, whereas the stored energy is proportional to the inhomogeneity length. Since the reflection coefficient remains constant for all inhomogeneity profiles, the linewidths of resonances increase with the decrease of t. For the same reason, the resonances at smaller I have smaller quality factors, since the boundary is more penetrable. In this case, the resonances are loaded more efficiently by waves leaving the inhomogeneity.

Thus, we have shown that the nonmonotonic behavior of $|T(I)|$ in the regime of scattering is due to resonant scattering. The maximum of transmission at nonzero I is formed by overlapping of neighboring resonances because of large resonance linewidths and the distribution of the resonances as a function of I. The former effect is connected with the small length of the resonator.

C. Transmission and incident wave number

We now examine how the amplitude of the transmission coefficient in the minimum of transmission seen in Fig. 4 increases with the value of incident wave number k_0. The calculations shown in Fig. 10 indicate that the quality factors of resonances as well as the differences between the neighboring resonances $|\mathrm{Re}(1/\lambda_{n+1})-\mathrm{Re}(1/\lambda_n)|$ decrease with increasing k_0. This gives a larger overlapping of neighboring resonance lines, and hence a smaller variation of transmission between maxima and minima. The reason for the increase of resonance linewidths is that there is a smaller relative change of the wave number $|(k_i-k_0)/k_0|$ for the same magnitude of inhomogeneity when k_0 becomes larger. (Here, k_i is the wave number inside the inhomogeneity [Fig. 1(c)].) A smaller magnitude of $|(k_i-k_0)/k_0|$ means a smaller reflection from the inhomogeneity edges and the wave is less trapped by the inhomogeneity, corresponding to a larger

resonance linewidth $|\mathrm{Im}(1/\lambda_n)|$ and hence less structure in the transmission resonances.

This phenomenon also has an analogy to quantum mechanics. In Ref. 33, it is shown that for the square potential, the amplitude of the transmitted wave in the minima of transmission between two consecutive resonances is proportional to $|E/V| = |-(\hbar k_0)^2/(2mV)|$. Thus, it grows with the wave number of the incident wave.

With the increase of $|E/V|$ for a given potential V [in our case, with the increase of the quantity $|(1+\upsilon_0)/I\delta\upsilon(z)|$ for given I], the particle's energy is farther above the top of the potential well $E-V=0$ [in our case, the quantity $1+\upsilon_0$ is farther from its value for the upper edge of BVMSW range inside the inhomogeneity $-I\delta\upsilon(z)$]. The quantity $|(E-V)/E|$ (BVMSW: $|[1+\upsilon_0+I\delta\upsilon(z)]/(1+\upsilon_0)|$) becomes closer to 1; therefore, $|(k_i-k_0)/k_0|$ becomes smaller. Therefore, the reflection from the well edges decreases, resulting in less pronounced minima of transmission.

Thus, with the increase of $1+\upsilon_0$, the initial wave number k_0 grows. Therefore, as the magnetostatic wave approaches the inhomogeneity, it is "energetically" farther from the prohibited zone $1+\upsilon_0<0$ and is less trapped as well as reflected back by the well.

D. Accumulated phase shift

Finally, we discuss the magnitude of the additional accumulated phase shift as a function of the applied current. As seen in Figs. 4 and 5, for positive current values, the experimental phase shift has a general tendency to decrease linearly with the current applied. We can obtain a simple formula for the phase shift in this region using the Wentzel-Kramers-Brillouin (WKB) approximation.[33]

We define the local wave number $k(z)$ as a solution of the local dispersion relation $\chi(z,\omega)^{-1}-W(|k(z)|)=0$, introduced above. With the same approximations used in Eqs. (B1) and (B15), we arrive at the expression for the local wave number. We find

$$k(z) = -\frac{2}{L}[1+\upsilon_0(\omega)+I\delta\upsilon(z,\omega)] = -|k_0| - \frac{2}{L}I\delta\upsilon(z,\omega). \tag{22}$$

Note that we accounted for the negative dispersion of BVMSW by putting a negative sign in front of the brackets. The additional accumulated phase is $\Delta\phi=\int_{-w/2}^{w/2}[k(z)-k_0]dz$. As a result, with the upper expression from Eq. (7), we arrive at an expression for $\Delta\phi$ in terms of I and the profile shape:

$$\Delta\phi = \frac{4\pi}{5L}\eta(\omega)I. \tag{23}$$

The dash-dot-dotted line in the lower panel of Fig. 5(b) shows the phase of the transmission coefficient calculated using Eq. (23). The linear dependence of the phase accumulated on the height of the inhomogeneity is well described by the WKB approximation. The additional phase shift accumulated is primarily connected to the modified wave number of the transmitted wave in the barrier.

We note that the numerical calculations shown in Fig. 5 are most nonlinear at small wave number. The greatest nonlinearity occurs at current magnitudes corresponding to maxima and minima of the transmission coefficient.

Our experiment showed that for the negative current direction, the phase shift behavior is very different. At small negative values of current, the phase shift remains linear in I, but is nonlinear at larger currents. This can now be understood by noting that at small negative I, the incident wave is scattered from the inhomogeneity and phase accumulation is due to a modified wave number while inside the inhomogeneity. Because of the negative BVMSW dispersion, a decrease of the wave number by the inhomogeneity causes the additional phase shift to be positive.

At larger negative current values, a zone prohibited for BVMSW propagation is formed. The zone length l_p is the root of the equation $\upsilon_0(\omega)+\delta\upsilon(l_p/2,\omega)I=-1$. The zone length grows with the strength of applied current following the law

$$l_p(I) = \sqrt{[(r+d)^2 - \exp[-\eta(\omega)I/(5L)](r+d+L)^2]/[\exp[-\eta(\omega)I/(5L)]-1]}$$

A plot of this is shown in the inset to Fig. 5(b). Since the inhomogeneity is smooth, in front of and behind the zone, there exist regions of reduced static field where the wave can propagate. In these two regions of allowed propagation, the wave accumulates a phase shift. Tunneling through the prohibited zone results in a negligible accumulated phase. A larger prohibited zone length does not therefore lead to a significant increase in phase shift. Hence, the dependence on current is not linear in this large current limit.

We now prove this idea with a short calculation. We use the following procedure to calculate the additional accumulated phase shift in the presence of the prohibited zone. As stated above, while deriving Eq. (22) from Eqs. (B1) and (B15), we assumed k in Eq. (B15) to be negative. The wave number $k(z)$ in Eq. (22) becomes positive for values of z which define boundaries for the prohibited zone. Assuming that the accumulated phase in the prohibited zone is zero, we estimate the additional accumulated phase shift by subtracting an integral over the range of positive $k(z)$ values from the integral in Eq. (23). This gives

$$\Delta\phi = \frac{2\eta(\omega)}{5L}\left[2\pi - \frac{1}{L}\int_{-l_p(I)/2}^{l_p(I)/2} Y(z)dz\right]I - k_0 l_p(I). \tag{24}$$

The function $Y(z)$ is positive everywhere. Hence, with the increase of the current, the dependence $\Delta\phi(I)$ [Eq. (24)] deviates from a straight line toward smaller $|\Delta\phi|$ values, which is in qualitative agreement with Fig. 4. We calculate the magnitude of the current I_t for which the prohibited zone begins to form. In the incident wave number range 50–200 rad/cm, I_t varies from −0.088 to −0.47 A. These values are in agreement with the change of curve character from linear to nonlinear in the lower panel of Fig. 4.

We also made calculations of the phase shift by using Eq. (24). As one sees in Fig. 5, the results are in good agreement with the rigorous solution of the integral equation.

Thus, in this section, we have shown that the experimentally observed linear behavior of the accumulated phase on the current applied for $I>0$ is primarily connected to the local variation of wave number in the potential well. The observed tendency of saturation of $\Delta\phi(I)$ for large $I<0$ is connected with zero phase accumulation in the prohibited zone and the growth of the length of the prohibited zone with I.

CONCLUSION

We have studied experimentally and theoretically the transmission of a dipole-dominated spin wave in a ferromagnetic film through a localized inhomogeneity in the form of magnetic field produced by a dc through a wire placed on the film surface. We show that the amplitude and phase can be simultaneously affected by the current induced field, a feature that will be relevant for logic based on spin wave transport.

The direction of the current creates either a barrier or a well for spin wave transmission. We experimentally found that the current dependence of the amplitude of spin wave transmitted through the well inhomogeneity is nonmonotonic. The dependence has a minimum and an additional maximum. The theory clarifies the origin of the maximum. It shows that the transmission of spin waves through the inhomogeneity can be considered as a scattering process and that the additional maximum is a scattering resonance.

A linear decrease of the phase of the transmitted wave on the height of the inhomogeneity was found experimentally in the regime of wave scattering from the field hump (well inhomogeneity). The theory and the experiment showed that the additional phase accumulation is primarily connected to the variation of spin wave number in the potential well. The nonmonotonic resonance behavior of amplitude and strong reflection from the barrier in the minimum of transmission do not result in a significant change of the overall character of the dependence. The phase dependence in the regime of wave scattering or tunneling through the field dip was found to deviate from linear behavior at a critical current. The critical current corresponds to the formation of a prohibited zone for spin wave propagation.

ACKNOWLEDGMENTS

This work was supported in part by the Deutsche Forschungsgemeinschaft and by the Australian Research Council.

APPENDIX A

To derive Eq. (1), we used a procedure as follows. First, we assume a harmonic oscillatory motion for the magnetization and the dynamic magnetic field,

$$\mathbf{m}(\mathbf{r},\omega)=\mathbf{m}(\mathbf{r})\exp(i\omega t),\quad \mathbf{h}(\mathbf{r},\omega)=\mathbf{h}(\mathbf{r})\exp(i\omega t). \tag{A1}$$

Also, we use a 1D Green's function representation for the dipole field of precessing magnetization in the film,

$$\mathbf{h}_d(z)=\mathbf{G}(z,z')\otimes\mathbf{m}(z), \tag{A2}$$

where $\otimes$ denotes the convolution operation and $\mathbf{h}_d(z)$ and $\mathbf{m}(z)$ are the dynamic dipole field and the dynamic magnetization averaged through the film thickness.[30] All the components of the tensorial Green's function $\mathbf{G}$ can be found in Ref. 30. For linear BVMSWs, only the diagonal component G_{xx} is important, since it is the only nonvanishing component, which induces a dipole field in the plane perpendicular to the direction of the film equilibrium magnetization. (Note that the in-plane component of the dynamic magnetization m_y, being parallel to BVMSW wave fronts, produces no dipole field if the film width tends to infinity compared to its thickness.)

Thus,

$$h_{dx}(z)=4\pi G_{xx}(z,z')\otimes m_x(z). \tag{A3}$$

On the other hand, the solution of the linearized Landau-Lifschitz equation has a form[28,29]

$$\mathbf{m}(z)=\hat{\boldsymbol{\chi}}(\omega,z)\mathbf{h}_{eff}(z). \tag{A4}$$

The effective dynamic field $\mathbf{h}_{\mathrm{eff}}$ in our case consists of the BVMSW dipole field and a microwave field of an external source exciting magnetization oscillations,

$$\mathbf{h}_{eff}(z)=\mathbf{h}_d(z)+\mathbf{h}_s(z). \tag{A5}$$

[Other possible contributions to $\mathbf{h}_{\mathrm{eff}}(z)$, if necessary, are taken into account in $\hat{\boldsymbol{\chi}}(\omega,z)$.]

The excitation source can be of different nature; it might be a microstrip antenna with a microwave current or a dynamic field of any inhomogeneity in the film, e.g., a dipole field of another wave in a region of inhomogeneous static magnetic field. In both cases, the external excitation field has only one component which affects the BVMSW dynamics. It is the x component. Therefore,

$$\mathbf{h}_{eff}=\mathbf{e}_x(h_{dx}+h_{sx}), \tag{A6}$$

where $\mathbf{e}_x$ is the unit vector in the x direction. With Eq. (A6), Eq. (A4) reduces to

$$m_x(z)=\chi(\omega,z)[h_{dx}(z)+h_{sx}(z)], \tag{A7}$$

or, taking into account Eq. (A3)

$$\chi(\omega,z)^{-1}m_x = 4\pi G_{xx}(z,z') \otimes m_x(z) + h_{sx}(z). \quad \text{(A8)}$$

Now, we specify the form of the external field $h_{sx}(z)$. We assume it to be the microwave magnetic field of a line source of infinitesimally small width in the direction z and situated at z_0. The amplitude of the microwave magnetic field is A. Under these assumptions, Eq. (A8) turns into Eq. (1).

APPENDIX B

Here, we derive the Green's function of excitation of dipole-dominated spin waves in a ferromagnetic film by an external source, which enters Eq. (1).

First, we make use of the fact that $\delta H_z(z) \ll H_s$ and expand the inverse of the diagonal component χ of the microwave susceptibility tensor:

$$\frac{\chi(z,\omega)^{-1}}{4\pi} = \upsilon_0(\omega) + \delta\upsilon(z,\omega)I + O\left[\left(\frac{I}{H_s}\right)^2\right], \quad \text{(B1)}$$

where

$$\upsilon_0(\omega) = \frac{\chi(z = \pm\infty,\omega)^{-1}}{4\pi} = \frac{\omega_H^2 - \omega^2}{\omega_H\omega_M} \quad \text{(B2)}$$

and

$$\delta\upsilon(z,\omega) = \eta(\omega)Y(z). \quad \text{(B3)}$$

Here,

$$\eta(\omega) = \frac{1}{H_s}\left[\frac{2\omega_H}{\omega_M} - \upsilon_0(\omega)\right], \quad \text{(B4)}$$

$\omega_H = \gamma H_s$, and $\omega_M = \gamma 4\pi M_S$, where $4\pi M_S = 1750$ Oe is the saturation magnetization of the YIG film used and $\gamma = 2.82 \times 10^6$ Hz/Oe.

If I is negative, $H(z)$ is reduced near the wire and $|\chi(z,\omega)^{-1}/(4\pi)|$ is increased in this region. A zone prohibited for BVMSW propagation exists where $|\chi(z,\omega)^{-1}/(4\pi)| > 1$. Tunneling can occur through this region, but not propagation.[22] If $|\chi(z,\omega)^{-1}|/(4\pi) < 1$ throughout the inhomogeneity region, an incident spin wave can scatter. This is realized for small $I > 0$ such that BVMSW propagation is allowed in the inhomogeneity region.

Using Eqs. (3)–(8), the integral equation of motion [Eq. (1)] becomes

$$-\upsilon_0(\omega)m(z) + \int_{-\infty}^{+\infty} G_{xx}(z,z')m(z')dz' = I\delta\upsilon(z,\omega)m(z) + A'\delta(z - z_0), \quad \text{(B5)}$$

where A' is a new constant specifying the amplitude of the incident wave.

The source terms on the right-hand side of Eq. (B5) are independent. The solution of Eq. (B5) is

$$m(z) = I\int_{-w/2}^{w/2} G_{exc}(z,z')\delta\upsilon(z',\omega)m(z')dz' + A'G_{exc}(z,z_0), \quad \text{(B6)}$$

where $G_{exc}(z,z')$ denotes the Green's function of excitation of dynamic magnetization by a point source located at z'.

If follows from Eq. (B5) that in the BVMSW case, it is the solution of equation, as follows:

$$[-\upsilon_0(\omega)\delta(z - z') + G_{xx}(z,z')] \otimes G_{exc}(z',z'') = \delta(z - z''). \quad \text{(B7)}$$

The homogeneous equation [cf. Eq. (B5)]

$$\upsilon_0(\omega)m^0(z) - \int_{-\infty}^{+\infty} G_{xx'}(z,z')m^0(z')dz' = 0 \quad \text{(B8)}$$

describes the BVMSW propagation in a homogeneously magnetized film. The equation represents an eigenvalue problem for the integral operator, in which $\upsilon_0(\omega)$ plays the role of the operator's eigenvalue. One easily finds that the operator has a continuous set of eigenfunctions in the form of traveling waves,

$$m^0(z) = \exp(ikz), \quad \text{(B9)}$$

with arbitrary real wave numbers k. Substitution of Eq. (B9) into the operator results in the expression for its eigenvalues $W(k)$:

$$W(k) = \frac{1}{|k|L}[\exp(-|k|L) - 1]. \quad \text{(B10)}$$

As seen from expression (B10), the set of eigenvalues is doubly degenerate, to each eigenvalue W correspond two eigenfunctions: $m^0(z) = \exp(i|k|z)$ and $m^0(z) = \exp(-i|k|z)$. The eigenfunctions represent two plane waves with frequency ω and wave numbers $|k|$ and $-|k|$, traveling in opposite directions. Substitution of Eqs. (B9) and (B10) into Eq. (B8) results in the dispersion relation for BVMSW,

$$\upsilon_0(\omega) - W(|k|) = 0. \quad \text{(B11)}$$

As the plane waves represent the eigensolutions of the homogeneous equation (B8), we search for the solution of the inhomogeneous equation (B7) in the form of a set of plane waves:

$$G_{exc}(z,z') = \int_{-\infty}^{\infty} g_k \exp[-ik(z - z')]dk. \quad \text{(B12)}$$

Then, taking into account the result in Eq. (B10), we obtain

$$G_{exc}(z,z') = \frac{1}{2\pi}\int_{-\infty}^{\infty} \frac{\exp[-ik(z - z')]}{W(|k|) - \upsilon_0(\omega)}dk. \quad \text{(B13)}$$

If $|k_0|$ is the wave vector value which satisfies dispersion relation (B11) for a given value of ω, then we can rewrite Eq. (B13) as follows:

$$G_{exc}(z,z') = \frac{1}{2\pi}\int_{-\infty}^{\infty} \frac{\exp[-ik(z - z')]}{W(|k|) - W(|k_0|) - i\upsilon_0''(\omega)}dk. \quad \text{(B14)}$$

Here, we phenomenologically introduced the magnetic losses by adding an imaginary part $\upsilon_0''(\omega)$ to $\upsilon_0(\omega) = \chi_0(z,\omega)^{-1}/(4\pi)$.

Note that υ_0'' is positive. This follows from the expression for the microwave magnetic susceptibility tensor in the presence of magnetic losses:[29] $\chi=\chi'-i\chi''$ and $\chi''>0$. Therefore, $\chi^{-1}=(\chi'+i\chi'')/(\chi'^2+\chi''^2)\equiv 4\pi(\upsilon'+i\upsilon')$ and $\upsilon'>0$.

The following condition is usually satisfied in experiments: $|k|L\ll 1$. Under this condition,

$$W(|k|)\approx\frac{|k|L}{2}-1. \tag{B15}$$

This result allows one to obtain Eq. (B14) in closed form,

$$G_{exc}(z,z')=\frac{1}{\pi L}[2\pi i\exp(ik_0^c|z-z'|)+\exp(ik_0^c|z-z'|)E_1(ik_0^c|z-z'|)+\exp(-ik_0^c|z-z'|)E_1(-ik_0^c|z-z'|)]. \tag{B16}$$

Here,

$$k_0^c=|k_0|+i\frac{2\upsilon_0''}{L} \tag{B17}$$

is the complex wave number of the wave excited by the source in a resonant way and $E_1(z)$ is the exponential integral. It has a series representation as $E_1(z)=-C-\ln(z)-\Sigma_{n=1}^{\infty}\frac{(-1)^n z^n}{nn!}$.[34]

The first term in the brackets of Eq. (B6) represents traveling waves propagating in both directions from the point source. The second term, singular along the line $z=z'$, represents the near (reactive) field of the source. The reactive field is localized at the source and exhibits no retardation. Far away from the excitation source, the reactive field vanishes and $G_{exc}(z,z')$ reduces to

$$G_{exc}(z,z')\cong\frac{2i}{L}\exp(ik_0^c|z-z'|),\quad |z-z'|\gg L. \tag{B18}$$

The last term of Eq. (B16) reduces to $B\exp(ik_0^c z)$, where B is a constant. B represents a normalized amplitude of the excitation source, and we can set B equal to 1 with no loss of generality. As a result, the equation of motion of magnetization [Eq. (B6)] takes its final form:

$$m(z)=I\int_{-w/2}^{w/2}G_{exc}(z,z')\delta\upsilon(z',\omega)m(z')dz'+\exp(ik_0^c z). \tag{B19}$$

An expression similar to expression (B18) was first obtained in a different way in Ref. 35. Note that the whole wave factor in the far zone is $\exp(ik_0^c|z-z'|)\exp(i\omega t)$ [cf. Eq. (A1)]. Hence, the wave excited at $z=-\infty$ and incident onto the inhomogeneity from the left side has the negative wave number $-|k_0|$, since it is $\exp[i(|k_0|+i2\upsilon_0''/L)z]$ rather than $\exp[-i(|k_0|+i2\upsilon_0''/L)z]$, which vanishes at $z=+\infty$. This unusual feature reflects the fact that BVMSW is a backward wave. Its phase velocity is anticollinear to its group velocity. The direction of wave propagation is the direction of its group velocity, which in a passive medium coincides with the direction of decay of its amplitude. Thus, in the direction of the group velocity, i.e., in the direction of incidence, the phase accumulated by BVSMW on a propagation path l $-|k_0|l$ is negative.

APPENDIX C

Here, we derive an explicit transmission formula for small I. It follows from the discussion above that in the vicinity of $I=0$, we may neglect contributions of the higher resonant term of the series in Eq. (11) and keep only the zero order λ_0. We then have

$$T\simeq\frac{\int_{-w/2}^{w/2}\exp(ik_0^c z)\phi_0(z)dz}{1-I\lambda_0}u_0(w/2). \tag{C1}$$

Reference to Fig. 7 tells us that the inhomogeneity profile of Eq. (B3) is a good approximation for the modulus of $\phi_0(z)$ and we set $\phi_0(z)=\delta\upsilon(z,\omega)\exp(ik_0|z|)$ for the phase. We can also approximate $u_0(w/2)\simeq N^2\exp(ik_0 w)$, where N is a constant determined by the normalization condition in Eq. (12). Because $|u_0(z)|$ is close to a constant, we use

$$N^2\simeq\int_{-w/2}^{w/2}\delta\upsilon(z,\omega)\exp(i2k_0|z|)dz \tag{C2}$$

as an estimation of the norm. Then again, approximating $u_0(z)$ by the constant function with the phase modulation $\exp(ik_0|z|)$ and using the biorthogonality condition [Eq. (12)], we obtain

$$\lambda_0=\frac{1}{N^2}\int_{-w/2}^{w/2}dz\,\delta\upsilon(z,\omega)\exp(ik_0|z|)\times\int_{-w/2}^{w/2}\delta\upsilon(z',\omega)G_{exc}(z,z')\exp(ik_0|z'|)dz'. \tag{C3}$$

The dash-dot-dotted lines in Fig. 8 show T given by Eq. (C1) along with the exact numerical results obtained using the eigenfunction expansion method. The $T(I)$ behavior at small I (both positive and negative) is well described by Eq. (C1). A discrepancy appears for large I such that $|I|\gg|\mathrm{Re}(1/\lambda_1)-\mathrm{Re}(1/\lambda_0)|$ because the tails of higher transmission resonance lines become comparable with that of the lowest one. This indicates a transition to the tunneling regime, since the simultaneous out-of-resonance excitation of all the eigenmodes describes forced motion of magnetization within the inhomogeneity, excited by a source at the inhomogeneity boundary.

*Permanent address: FET Department, St. Petersburg Electrotechnical University, St. Petersburg 197376, Russia. kostylev@cyllene.uwa.edu.au

†serga@physik.uni-kl.de

[1] *Spin Dynamics in Confined Magnetic Structures I*, edited by B. Hillebrands and K. Ounadjela (Springer, Berlin, 2002); *Spin Dynamics in Confined Magnetic Structures II*, edited by B. Hillebrands and K. Ounadjela (Springer, Berlin, 2003); *Spin Dynamics in Confined Magnetic Structures III*, edited by B. Hillebrands and A. Thiaville (Springer, Berlin, 2006).

[2] A. O. Adeyeye and M. E. Welland, Appl. Phys. Lett. **80**, 2344 (2002).

[3] L. J. Heidemann, H. H. Solak, C. David, D. David, R. P. Cowburn, and F. Nolting, Appl. Phys. Lett. **85**, 4989 (2004).

[4] J. Shibata, K. Shigeto, and Y. Otani, J. Magn. Magn. Mater. **272-276**, 1688 (2004).

[5] P. Politi and M. G. Pini, Phys. Rev. B **66**, 214414 (2002); R. Arias and D. L. Mills, *ibid.* **67**, 094423 (2003).

[6] A. Yu. Galkin, B. A. Ivanov, and C. E. Zaspel, J. Magn. Magn. Mater. **286**, 351 (2005).

[7] P. Chu, D. L. Mills, and R. Arias, Phys. Rev. B **73**, 094405 (2006).

[8] G. Gubbiotti, S. Tacchi, G. Carlotti, P. Vavassori, N. Singh, S. Goolaup, A. O. Adeyeye, A. Stashkevich, and M. Kostylev, Phys. Rev. B **72**, 224413 (2005).

[9] A. V. Vashkovsky, V. I. Zubkov, E. H. Lock, and V. I. Scheglov, IEEE Trans. Magn. **26**, 1480 (1990).

[10] A. V. Vashkovskii and E. G. Lock, Phys. Usp. **47**, 601 (2004).

[11] A. V. Vashkovskii and E. G. Lock, Phys. Usp. **49**, 389 (2006).

[12] V. I. Zubkov and V. I. Scheglov, J. Commun. Technol. Electron. **46**, 1356 (2001).

[13] A. V. Vashkovskii, A. V. Voronenko, V. I. Zubkov, and V. N. Kil'dishev, Sov. Tech. Phys. Lett. **9**, 627 (1983).

[14] T. Cheng, H. S. Tuan, and J. P. Parekh, Proc.-IEEE Ultrason. Symp. **1**, 175 (1984).

[15] N. Guan, K. Yashiro, and S. Ohkawa, IEICE Trans. Electron. **E80-C**, 1388 (1997).

[16] K. Yashiro and S. Okawa, J. Appl. Phys. **53**, 3176 (1982).

[17] G. A. Vugalter, Sov. Phys. Tech. Phys. **28**, 23 (1983).

[18] Yu. I. Bespiatykh, I. E. Dikshtein, and A. D. Simonov, Sov. Phys. Tech. Phys. **34**, 136 (1989).

[19] V. E. Babenko, A. M. Mednikov, Yu. K. Milyaev, V. I. Melko, A. F. Popkov, V. G. Sorokin, and V. M. Shabunin, Sov. Phys. Tech. Phys. **31**, 221 (1986).

[20] S. V. Gerus and V. D. Kharitonov, Phys. Met. Metallogr. **58**, 1069 (1984).

[21] P. A. Kolodin and B. Hillebrands, J. Magn. Magn. Mater. **161**, 199 (1996).

[22] S. O. Demokritov, A. A. Serga, A. Andre, V. E. Demidov, M. P. Kostylev, B. Hillebrands, and A. N. Slavin, Phys. Rev. Lett. **93**, 047201 (2004).

[23] R. Hertel, W. Wulfhekel, and J. Kirschner, Phys. Rev. Lett. **93**, 257202 (2004).

[24] M. P. Kostylev, A. A. Serga, T. Schneider, B. Leven, and B. Hillebrands, Appl. Phys. Lett. **87**, 153501 (2005).

[25] R. W. Damon and J. R. Eshbach, J. Phys. Chem. Solids **19**, 308 (1961).

[26] I. Laulicht, J. T. Suss, and J. Barak, J. Appl. Phys. **70**, 2251 (1991).

[27] A. A. Serga, S. O. Demokritov, B. Hillebrands, and A. N. Slavin, J. Appl. Phys. **93**, 8758 (2003).

[28] D. Polder, Philos. Mag. **40**, 99 (1940).

[29] A. G. Gurevich and G. A. Melkov, *Magnetization Oscillations and Waves* (CRC, New York, 1996).

[30] K. Yu. Guslienko, S. O. Demokritov, B. Hillebrands, and A. N. Slavin, Phys. Rev. B **66**, 132402 (2002).

[31] E. Merzbacher, *Quantum Mechanics* (Wiley, New York, 1998), Chap. 13.

[32] L. D. Landau and E. M. Lifschitz, *Course of Theoretical Physics* (Pergamon, New York, 1977), Vol. 3.

[33] E. Merzbacher, *Quantum Mechanics* (Wiley, New York, 1998), Sec. 6.4.

[34] *Handbook of Mathematical Functions: with Formulas, Graphs, and Mathematical Tables*, edited by M. Abramovitz and I. A. Stegun (Dover Publications, New York, 1965).

[35] B. A. Kalinikos, Sov. Phys. J. **24**, 719 (1981).